J. Am. Soc. Mass Spectrom. (2017) 28:2344–2351
DOI: 10.1007/s13361-017-1745-5

RESEARCH ARTICLE

Improved Precision and Accuracy of Quantification of Rare Earth Element Abundances via Medium-Resolution LA-ICP-MS

Rebecca Funderburg,[1] Ricardo Arevalo Jr.,[2] Marek Locmelis,[3] Tomoko Adachi[2]

[1]Texas Christian University, Fort Worth, TX 76129, USA
[2]NASA Goddard Space Flight Center, Greenbelt, MD 20771, USA
[3]Department of Geosciences and Geological and Petroleum Engineering, Missouri University of Science and Technology, Rolla, MO 65409, USA

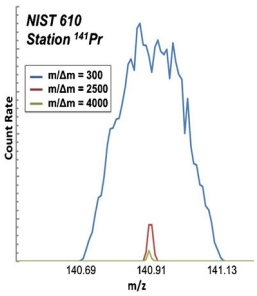

Abstract. Laser ablation ICP-MS enables streamlined, high-sensitivity measurements of rare earth element (REE) abundances in geological materials. However, many REE isotope mass stations are plagued by isobaric interferences, particularly from diatomic oxides and argides. In this study, we compare REE abundances quantitated from mass spectra collected with low-resolution (m/Δm = 300 at 5% peak height) and medium-resolution (m/Δm = 2500) mass discrimination. A wide array of geological samples was analyzed, including USGS and NIST glasses ranging from mafic to felsic in composition, with NIST 610 employed as the bracketing calibrating reference material. The medium-resolution REE analyses are shown to be significantly more accurate and precise (at the 95% confidence level) than low-resolution analyses, particularly in samples characterized by low (<μg/g levels) REE abundances. A list of preferred mass stations that are least susceptible to isobaric interferences is reported. These findings impact the reliability of REE abundances derived from LA-ICP-MS methods, particularly those relying on mass analyzers that do not offer tuneable mass-resolution and/or collision cell technologies that can reduce oxide and/or argide formation.

Keywords: Precision, Laser ablation, Magnetic sector LA-ICP-MS, Rare earth elements

Received: 22 March 2017/Revised: 12 June 2017/Accepted: 15 June 2017/Published Online: 10 July 2017

Introduction

The rare earth elements (REE; i.e., La through Lu), share a common electronic structure: [Xe] $6s^2$ $5d^x$ $4f^y$, where $1 \geq x \geq 0$ and $0 \geq y \geq 14$. Consequently, under many environmental conditions found on Earth (e.g., pressure, temperature, and importantly oxygen fugacity), these elements form trivalent cations (i.e., M^{3+}, commonly from the loss of one 4f and two 6s electrons) chemical behaviors of which are controlled primarily by systematic variations in their respective ionic radii. In the Earth sciences, the predictable geochemical behaviors of the REE can be and is commonly exploited to identify magma source contributions, discern geographical provenances, and characterize environmental conditions and geological processes, including (but not limited to):

- Distinction of respective sources of mantle- and crustal-derived materials through proxies like Ce/Pb, Ti/Eu, Y/Ho, and Sr/Nd ratios (e.g., Hofmann, 2003 [1]; Workman and Hart, 2005 [2]; Arevalo and McDonough, 2010) [3], and identification of source lithology and/or specific mineralogy via diagnostic chemical signatures, such as the characteristic depression in the normalized abundances of heavy REE observed in derivatives of garnet-bearing peridotite (White, 2013) [4];
- Depletion of incompatible elements (e.g., light REE relative to heavy REE) due to multiple episodes of partial melting and melt extraction (e.g., Hofmann, 1988) [5], or enrichment in incompatible elements via low degrees of melting (e.g., Sun and McDonough, 1989) [6], crustal contamination (McDonough, 1990) [7] and/or metasomatic overprinting (McKenzie, 1989) [8];

Electronic supplementary material The online version of this article (doi:10.1007/s13361-017-1745-5) contains supplementary material, which is available to authorized users.

Correspondence to: Rebecca Funderburg; *e-mail:* rebeccaf219@gmail.com

- Classification of calcium aluminum inclusions (CAIs) and other refractory meteorite phases from patterns of normalized REE abundances (MacPherson et al. 1988) [9], and fractionation of refractory and volatile solar system materials during planetary accretion (Dauphas et al. 2015) [10];
- Determination of oxidation states, and reconstructions of local oxygen fugacity (fO_2) levels, based on Ce and Eu concentration anomalies preserved in magmatic zircons, caused by redox-sensitive valence states of Ce (3+/4+) and Eu (2+/3+) (Trail et al. 2012) [11]; and,
- Identification of economically viable ores of REE, which are commonly exploited for catalysts, such as automotive catalytic converters; battery alloys; high-strength permanent magnets; glassmaking and polishing compounds; and light-emitting diodes (LEDs) (Goonan 2011) [12].

The measurement and quantification of REE abundances in geological and/or planetary materials with high precision and accuracy are essential to addressing these science objectives with confidence, particularly as most rocks and minerals only contain a few μg/g (or less) levels of these elements.

REE abundances are routinely measured on quadrupole inductively coupled plasma mass spectrometer (ICP-MS) equipment. However, these instruments offer only limited mass resolving powers (typically $m/\Delta m < 500$ at 5% peak intensity), restricting their ability to distinguish targeted mass peaks from potential isobaric interferences that occur when two or more atomic and/or molecular species have overlapping mass-to-charge (m/z) ratios. During the analysis of REE abundances in common geological materials, such isobaric interferences occur primarily as elemental interferences, such as ^{142}Nd at mass station ^{142}Ce; diatomic oxides, such as $^{126}Te^{16}O$ at ^{142}Ce; and diatomic argides, such as $^{102}Ru^{40}Ar$ at ^{142}Ce.

Double-focusing sector field instruments that offer adjustable mass discrimination may isolate these potential interferences, albeit at the expense of sensitivity. Collision induced dissociation (CID) cells reduce oxide and argide formation with varying degrees of efficacy, but CID cannot differentiate competing elemental isobars or double-charged interferences. Further, CID cells are normally only found on quadrupole ICP-MS instruments; sector field instruments are rarely equipped with this hardware. Thus, the method pioneered here could be used in concert with or in lieu of a CID cell.

As such, the primary objective of this study is to determine if medium mass-resolution ($m/\Delta m > 500$ at 5% peak intensity) is required for the highest precision/accuracy measurements of REE in a range of mantle-derived materials.

Instrumentation and Operating Conditions Employed for This Study

A suite of geological reference materials (Figure 1), described further below, was analyzed at NASA Goddard Space Flight Center using a Nu Instruments AttoM single-collector ICP-MS. This instrument offers tuneable mass-resolution from $m/\Delta m = 300$ up to 10,000 (measured at 5% of the maximum peak intensity), and was coupled to a Photon Machines Ultra Short Pulse Analyte G2 (ArF excimer) laser system that generates 193 nm radiation with energy densities up to >15 J/cm^2, pulse widths of <4 ns, and repetition rates up to 300 Hz. Elemental abundances were measured using low- and medium-resolution mass discrimination (i.e., $m/\Delta m = 300$ and $m/\Delta m = 2500$, respectively). All other parameters (e.g., laser fluence/shots, gas flow rates, forward power, etc.; Appendix I) were held constant in order to unambiguously identify and isolate potential isobaric interferences on each monitored isotope mass station (Table 1). Multiple mass stations for each element were analyzed in order to verify terrestrial isotope ratios in the absence of obvious isobars.

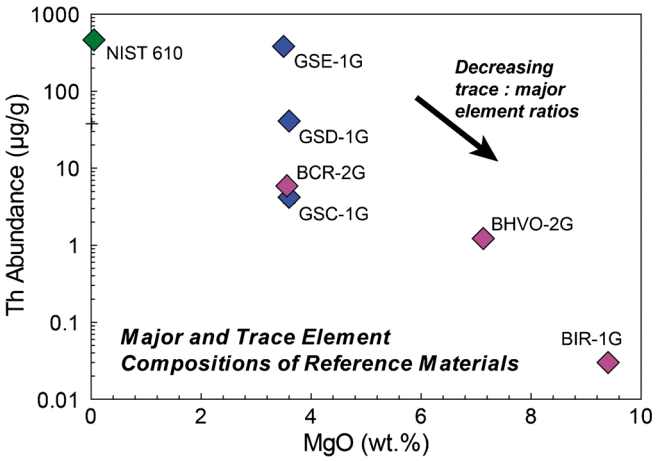

Figure 1. Compositional characterization of the reference materials analyzed here, which span several orders of magnitude in trace element abundances (as represented by Th). According to the International Union of Geological Sciences (IUGS), the USGS glasses BHVO-2G and BIR-1G are classified as basalts, BCR-2G as a basaltic andesite, and the GSC, GSD, and GSE glasses as trachyandesites. According to the same standards, NIST SRM 610 is rhyolitic in composition

Low mass resolving powers (i.e., $m/\Delta m = 300$) are commonly associated with commercial quadrupole mass spectrometers, and considered to be the default for sector field instruments. However, a higher mass resolving power of $m/\Delta m = 2500$ was chosen for this study in order to enable the separation of key isobaric interferences (e.g., those with high abundances and/or high molecular formation efficiencies) while preserving maximum ion transmission/signal intensity, and by extension, instrument sensitivity. This specific mass resolving power was determined to be the lowest acceptable setting given probabilities of oxide and argide formation (typically <0.20% and <0.01%, respectively), and expected cation concentrations found in common geological materials (Table 2). Potential isobars that remain irresolvable at a mass resolving power of $m/\Delta m = 2500$ (5% peak height) are generally characterized by expected abundances several orders of magnitude below those expected across the explored range of terrestrial compositions (Appendix II). For reference, given prototypical peak shapes/kurtosis at $m/\Delta m = 2500$ at 5% of the maximum peak height,

Table 1. Measured Isotope Mass Stations, Abundances, and Potential Isobaric Interferences During Nominal LA-ICP-MS Analysis

Element	Isotope	Mass station (Da)	Relative abundance	Hydrides (MH)	Oxides[a] ($M^{16}O$)	Argides ($M^{36}Ar$)	Argides ($M^{38}Ar$)	Argides ($M^{40}Ar$)	Monoatomic interferences
La	^{138}La	137.91	0.1%	^{137}Ba	^{122}Sn, ^{122}Te	^{102}Ru, ^{102}Pd	^{100}Mo	^{98}Mo, ^{98}Ru	^{138}Ba, ^{138}Ce
	^{139}La	138.91	99.9%	^{138}Ce, ^{138}La, ^{138}Ba	^{123}Sb, ^{123}Te	^{103}Rh	^{101}Ru	^{99}Ru	
Ce	^{140}Ce	139.91	88.5%	^{139}La	^{124}Sn, ^{124}Te, ^{124}Xe	^{104}Ru, ^{104}Pd	^{102}Ru, ^{102}Pd	^{100}Mo, ^{100}Ru	
	^{142}Ce	141.91	11.1%	^{141}Pr	^{126}Te, ^{126}Xe	^{106}Pd	^{102}Ru, ^{102}Pd	^{102}Ru, ^{102}Pd	^{142}Nd
Pr	^{141}Pr	140.91	100.0%	^{140}Ce	^{125}Te	^{105}Pd	^{103}Rh	^{101}Ru	
Nd	^{142}Nd	141.91	27.2%	^{141}Pr	^{126}Te, ^{126}Xe	^{106}Pd	^{104}Ru, ^{104}Pd	^{102}Ru, ^{102}Pd	^{142}Ce
	^{144}Nd	143.91	23.8%	^{143}Nd	^{128}Te, ^{128}Xe	108Pd, ^{108}Cd	^{106}Pd	^{104}Ru, ^{104}Pd	^{144}Sm
	^{146}Nd	143.91	17.2%	^{145}Nd	^{130}Te, ^{130}Ba, ^{130}Xe	^{110}Pd, ^{110}Cd	^{108}Pd, 108Cd	^{106}Pd	
Sm	^{147}Sm	146.91	15.0%	^{146}Nd	^{131}Xe	^{110}Pd, ^{110}Cd	^{109}Ag	^{107}Ag	
	^{152}Sm	151.92	26.8%	^{151}Eu	^{136}Xe, ^{136}Ba, ^{136}Ce	^{116}Cd, ^{116}Sn	^{114}Cd, ^{114}Sn	^{112}Cd, ^{112}Sn	^{152}Gd
	^{154}Sm	153.92	22.8%	^{153}Eu	^{138}Ba, ^{138}La, ^{138}Ce	^{118}Sn	^{116}Cd, ^{116}Sn	^{114}Cd, ^{114}Sn	^{154}Gd
Eu	^{151}Eu	150.92	47.8%	^{150}Sm	^{135}Ba	^{115}In, ^{115}Sn	^{113}Cd, ^{113}In	^{111}Cd	
	^{153}Eu	152.92	52.2%	^{152}Sm	^{137}Ba	^{117}Sn	^{115}In, ^{115}Sn	^{113}Cd, ^{113}In	
Gd	^{156}Gd	155.92	20.5%	^{155}Gd	^{140}Ce	^{120}Sn, ^{120}Te	^{118} Sn	^{116}Cd, ^{116}Sn	^{156}Dy
	^{158}Gd	157.92	24.8%	^{157}Gd	^{142}Ce, ^{142}Nd	^{122}Sn, ^{122}Te	^{120}Sn, ^{120}Te	^{118}Sn	^{158}Dy
Tb	^{159}Tb	159.93	100.0%	^{158}Gd	^{143}Nd	^{123}Sb, ^{123}Te	^{121}Sb	^{119}Sn	
Dy	^{162}Dy	161.93	25.5%	^{161}Dy	^{146}Nd	^{126}Te, ^{126}Xe	^{124}Sn, ^{124}Te, ^{124}Xe	^{122}Sn, ^{122}Te	^{162}Er
	^{163}Dy	162.93	24.9%	^{162}Dy, ^{162}Er	^{147}Sm	^{127}I	^{125}Te	^{123}Sb, ^{123}Te	
	^{164}Dy	163.93	28.2%	^{163}Dy	^{148}Nd, ^{148}Sm	^{128}Te, ^{126}Xe	^{126}Te, ^{126}Xe	^{124}Sn, ^{124}Te, ^{124}Xe	^{164}Er
Ho	^{165}Ho	164.93	100.0%	^{164}Dy, ^{164}Er	^{149}Sm	^{127}I	^{127}I	^{125}Te	
Er	^{166}Er	165.93	33.6%	^{165}Ho	^{150}Nd, ^{150}Sm	^{130}Te, ^{130}Ba, ^{130}Xe	^{128}Te, ^{126}Xe	^{126}Te, ^{126}Xe	
	^{167}Er	166.93	22.9%	^{166}Er	^{151}Eu	^{131}Xe	^{129}Xe	^{127}I	
	^{168}Er	167.93	26.8%	^{167}Er	^{152}Sm, ^{152}Gd	^{132}Ba, ^{132}Xe	^{130}Te, ^{130}Ba, ^{130}Xe	^{128}Te, ^{126}Xe	
Tm	^{169}Tm	169.94	100.0%	^{168}Er	^{153}Eu	^{133}Cs	^{131}Xe	^{129}Xe	
Yb	^{171}Yb	170.94	14.3%	^{170}Er	^{155}Gd	^{135}Ba	^{133}Cs	^{131}Xe	
	^{172}Yb	171.94	21.8%	^{171}Yb	^{156}Gd, ^{156}Dy	^{136}Xe, ^{136}Ba, ^{136}Ce	^{134}Xe, ^{134}Ba	^{132}Ba, ^{132}Xe	
	^{173}Yb	172.94	16.1%	^{172}Yb	^{157}Gd	^{137}Ba	^{135}Ba	^{133}Cs	
Lu	^{175}Lu	174.94	97.4%	^{174}Yb	^{159}Tb	^{139}La	^{137}Ba	^{135}Ba	
	^{176}Lu	175.94	2.6%	^{175}Lu	^{160}Gd, ^{160}Dy	^{140}Ce	^{138}Ba, ^{138}La, ^{138}Ce	^{136}Xe, ^{136}Ba, ^{136}Ce	^{176}Yb
Hf	^{177}Hf	176.94	18.6%	^{176}Hf	^{161}Dy	^{141}Pr	^{139}La	^{137}Ba, ^{137}La, 137Ce	
	^{178}Hf	177.94	27.3%	^{177}Hf	^{162}Dy, ^{162}Er	^{142}Ce, ^{142}Nd	^{140} Ce	^{138}Ba, ^{138}La, ^{138}Ce	
	^{180}Hf	179.95	35.1%	^{179}Hf	^{164}Dy	^{144}Sm, ^{144}Nd	^{142}Ce, ^{142}Nd	^{140}Ce	

[a] Diatomic oxides $M^{17}O$ and $M^{18}O$ represent much lower risks of serving as isobaric interferences due to their limited isotopic abundances (i.e., $^{17}O/^{16}O \approx 10^{-4}$, $^{18}O/^{16}O \approx 10^{-3}$), and the low oxide production rates (i.e., ThO/Th < 0.20%) supported by the method described here

competing isobars may be resolved at an equivalent resolution of $m/\Delta m \approx 3300$ at full width of half maximum (FWHM) of the peak height, enabling high-fidelity spectral quantitation via peak top comparisons and/or smaller peak area integration windows (Table 2; Appendix III).

Prior to each daily run of analyses, the ion lenses and the position of the torch of the ICP-MS were tuned to maximize signal (based on ^{238}U spectra) and minimize oxide production (ThO/Th < 0.20%) first in low-resolution ($m/\Delta m = 300$, 5% peak height), then in medium-resolution ($m/\Delta m = 2500$, 5% peak height). A three-stage mass calibration technique was used to calibrate the magnet for accurate peak scanning: the first calibration was completed in low-resolution with a wide search window, then in medium-resolution with a wide search window, and finally in medium-resolution with a narrow search window. Peak shapes were verified individually and the scanning deflectors were calibrated prior to each run. The spot size for both low- and medium-resolution scans was held constant (diameter = 150 μm) in order to circumvent disproportionate laser-induced elemental fraction (LIEF) associated with laser pit aspect ratios (driven by the efficiency by which particles can be extracted from the ablation site), and ultimately allow for a direct comparison between low- and medium-resolution techniques.

The complete list of mass stations monitored in this study is provided in Table 2, along with the most likely monoatomic and diatomic isobaric inferences introduced during laser processing of oxygen-rich geological materials in an ambient He environment, and sample injection into an argon plasma torch. Elemental abundances were quantified for $^{138, 139}$La, $^{140, 142}$Ce, ^{141}Pr, $^{142, 144, 146}$Nd, $^{147, 152, 154}$Sm, $^{151, 153}$Eu, $^{156, 158}$Gd, ^{159}Tb, $^{162, 163, 164}$Dy, ^{165}Ho, $^{166, 167, 168}$Er, ^{169}Tm, $^{172, 173}$Yb, $^{175, 176}$Lu, and $^{177, 178, 180}$Hf, with ^{178}Hf serving as the internal standard. Detection parameters are outlined in the Appendix.

Prior to each analysis, a blank signal was collected for 30 s with the laser firing but the shutter closed to collect a background signal with all sources of electronic noise present, including Johnson, flicker, and shot varieties. The background signal was subtracted from the analyte signal for data quantitation. Helium was used as the carrier gas at a flow rate of 1.00 L/min because of its higher ionization potential relative to other carrier gas options (Russo 1995) [17]; all ablations occurred in an ambient He atmosphere within the laser cell; the gas dynamics at the ablation site, as driven by the gas flow rate and the HelEx high-performance two-volume sample cell, achieved >99% signal washout within less than a single s, thereby maximizing spatial resolution (including depth profiling). Between the ablation of each sample and reference material, the

Table 2. Recommended Mass Stations for REE Analysis via LA-ICP-MS Methods, and Model Compositions of Common Geological Materials to Which This Method May Be Applied

Preferred isotope	Relative abundance	Interferences[a] at resolution (m/Δm = 300, 5%)	Interferences[a] at resolution (m/Δm = 1500, 5%)	Interferences[a] a resolution (m/Δm = 2500, 5%)	*Relevant interferences[a,b] above m/Δm = 2500 (5%)*	Representative compositions of common geological materials (in μg/g)								
						CI Chondrite[c]	MORB[d]	OIB[e]	BCC[f]	Basalt Zircon[g]	Granitoid Zircon[g]	Kimberlite Zircon[g]	Lamproite Zircon[g]	Carbonatite Zircon[g]
^{139}La	99.9%	^{138}CeH, ^{138}LaH, ^{138}BaH, $^{123}Sb^{16}O$, $^{123}Te^{16}O$, $^{99}Ru^{40}Ar$	^{138}CeH, ^{138}LaH, ^{138}BaH, $^{123}Sb^{16}O$, $^{123}Te^{16}O$, $^{99}Ru^{40}Ar$	^{138}CeH, ^{138}LaH, ^{138}BaH, $^{123}Te^{16}O$	*None*	0.25	3.8	37	20	-	12	<0.09	<0.20	0.17
^{140}Ce	88.5%	^{139}LaH, $^{124}Se^{16}O$, $^{124}Te^{16}O$, $^{124}Xe^{16}O$, $^{100}Mo^{40}Ar$, $^{100}Ru^{40}Ar$	^{139}LaH, $^{124}Se^{16}O$, $^{124}Te^{16}O$, $^{124}Xe^{16}O$, $^{100}Mo^{40}Ar$, $^{100}Ru^{40}Ar$	^{139}LaH, $^{124}Se^{16}O$, $^{124}Te^{16}O$, $^{124}Xe^{16}O$	*None*	0.64	12	80	43	2.1	61	0.87	7.9	4.5
^{141}Pr	100%	^{140}CeH, $^{125}Te^{16}O$, $^{101}Ru^{40}Ar$	^{140}CeH, $^{125}Te^{16}O$, $^{101}Ru^{40}Ar$	^{140}CeH, $^{125}Te^{16}O$	*None*	0.10	1.7	9.7	4.9	0.08	8	<0.08	0.15	0.54
^{144}Nd	23.8%	^{143}NdH, $^{128}Te^{16}O$, $^{128}Xe^{16}O$, $^{104}Ru^{40}Ar$, $^{104}Pd^{40}Ar$, ^{144}Sm	^{143}NdH, $^{128}Te^{16}O$, $^{128}Xe^{16}O$, $^{104}Ru^{40}Ar$, $^{104}Pd^{40}Ar$, ^{144}Sm	^{143}NdH, $^{128}Te^{16}O$, $^{128}Xe^{16}O$, ^{144}Sm	*^{144}Sm*	0.47	9.8	39	20	0.90	45	0.39	1.8	6.2
^{154}Sm	22.8%	^{153}EuH, $^{138}Ba^{16}O$, $^{138}La^{16}O$, $^{138}Ce^{16}O$, $^{114}Cd^{40}Ar$, $^{114}Sn^{40}Ar$, ^{154}Gd	^{153}EuH, $^{138}Ba^{16}O$, $^{138}La^{16}O$, $^{138}Ce^{16}O$, $^{114}Cd^{40}Ar$, $^{114}Sn^{40}Ar$, ^{154}Gd	^{153}EuH, $^{138}Ba^{16}O$, $^{138}La^{16}O$, $^{138}Ce^{16}O$, ^{154}Gd	*$^{138}Ba^{16}O$, $^{138}Ce^{16}O$, ^{154}Gd*	0.15	3.3	10	3.9	1.8	22	0.53	3.3	6.6
^{153}Eu	52.2%	^{152}SmH, $^{137}Ba^{16}O$, $^{113}Cd^{40}Ar$, $^{113}Ir^{40}Ar$	^{152}SmH, $^{137}Ba^{16}O$, $^{113}Cd^{40}Ar$, $^{113}Ir^{40}Ar$	^{152}SmH, $^{137}Ba^{16}O$	*$^{137}Ba^{16}O$*	0.06	1.2	3.0	1.1	1.6	2.1	0.36	0.50	4.0
^{158}Gd	24.8%	^{157}GdH, $^{142}Ce^{16}O$, $^{142}Nd^{16}O$, $^{118}Sn^{40}Ar$, ^{158}Dy	^{157}GdH, $^{142}Ce^{16}O$, $^{142}Nd^{16}O$, $^{118}Sn^{40}Ar$, ^{158}Dy	^{157}GdH, $^{142}Ce^{16}O$, $^{142}Nd^{16}O$, ^{158}Dy	*$^{1142}Ce^{16}O$, $^{142}Nd^{16}O$, ^{158}Dy*	0.20	4.4	7.6	3.7	11	58	1.5	15	20
^{159}Tb	100%	^{158}GdH, $^{143}Nd^{16}O$, $^{119}Sn^{40}Ar$	^{158}GdH, $^{143}Nd^{16}O$, $^{119}Sn^{40}Ar$	^{158}GdH, $^{143}Nd^{16}O$	*$^{143}Nd^{16}O$*	0.04	0.74	1.1	0.60	-	-	-	-	-
^{163}Dy	24.9%	^{162}DyH, $^{147}Sm^{16}O$, $^{123}Sb^{40}Ar$, $^{123}Te^{40}Ar$, ^{158}Dy	^{162}DyH, $^{147}Sm^{16}O$, $^{123}Sb^{40}Ar$, $^{123}Te^{40}Ar$, ^{158}Dy	^{162}DyH, $^{147}Sm^{16}O$, ^{158}Dy	*$^{147}Sm^{16}O$*	0.25	5.1	5.6	3.6	35	225	4.1	37	56
^{165}Ho	100%	^{164}DyH, ^{164}ErH, $^{149}Sm^{16}O$, $^{145}Te^{40}Ar$	^{164}DyH, ^{164}ErH, $^{149}Sm^{16}O$, $^{145}Te^{40}Ar$	^{164}DyH, ^{164}ErH, $^{149}Sm^{16}O$	*$^{149}Sm^{16}O$*	0.06	1.1	1.1	0.77	15	85	1.3	14	15
^{167}Er	22.9%	^{166}ErH, $^{151}Eu^{16}O$, $^{127}I^{40}Ar$	^{166}ErH, $^{151}Eu^{16}O$, $^{127}I^{40}Ar$	^{166}ErH, $^{151}Eu^{16}O$	*$^{151}Eu^{16}O$*	0.17	3.2	2.6	2.1	65	378	4.3	63	53
^{169}Tm	100%	^{168}ErH, $^{153}Eu^{16}O$, $^{129}Xe^{40}Ar$	^{168}ErH, $^{153}Eu^{16}O$, $^{129}Xe^{40}Ar$	^{168}ErH, $^{153}Eu^{16}O$	*$^{153}Eu^{16}O$*	0.03	0.45	0.35	0.28	-	-	-	-	-
^{172}Yb	21.8%	$^{156}Gd^{16}O$, $^{156}Dy^{16}O$, $^{132}Ba^{40}Ar$, $^{132}Xe^{40}Ar$	$^{156}Gd^{16}O$, $^{156}Dy^{16}O$, $^{132}Ba^{40}Ar$, $^{132}Xe^{40}Ar$	$^{156}Gd^{16}O$, $^{156}Dy^{16}O$	*$^{156}Gd^{16}O$*	0.17	3.0	2.2	1.9	118	769	5.6	126	64
^{175}Lu	97.4%	^{174}YbH, $^{159}Tb^{16}O$, $^{135}Ba^{40}Ar$	^{174}YbH, $^{159}Tb^{16}O$, $^{135}Ba^{40}Ar$	^{174}YbH, $^{159}Tb^{16}O$	*$^{159}Tb^{16}O$*	0.03	0.45	0.30	0.30	25	150	1.1	28	11
^{178}Hf	27.3%	^{177}HfH, $^{162}Dy^{16}O$, $^{162}Er^{16}O$, $^{138}Ba^{40}Ar$, $^{138}La^{40}Ar$, $^{138}Ce^{40}Ar$	^{177}HfH, $^{162}Dy^{16}O$, $^{162}Er^{16}O$, $^{138}Ba^{40}Ar$, $^{138}La^{40}Ar$, $^{138}Ce^{40}Ar$	^{177}HfH, $^{162}Dy^{16}O$, $^{162}Er^{16}O$	*$^{162}Er^{16}O$*	0.11	2.4	7.8	3.7	6100	12800	13100	10000	10400

[a] Listed interferences cannot be resolved at either 5% of the maximum peak height or full width at half maximum (FWHM) of the peak intensity
[b] Irresolvable monoatomic interferences and diatomic oxides and argides with expected cation abundances within a factor of 100 of the targeted analyte (given the range of terrestrial compositions provided in this table).
[c] CI carbonaceous chondrite composition from Palme and Jones [13]
[d] Global mid-ocean ridge basalt (MORB) composition from Arevalo and McDonough [3]
[e] Ocean island basalt (OIB) composition from Sun and McDonough [14]
[f] Bulk continental crust (BCC) model composition from Rudnick and Gao [15]
[g] Median compositions of zircons from a range of rock types from Belousova et al. [16]

ablation system was flushed with He gas for 30 s to statistically eliminate any memory effects and/or hysteresis.

Data Processing

For all analyses, NIST 610 served as the standard; values for the major, minor, and trace element composition of this material were taken from Jochum et al. [18]. Raw data were collected using the Nu AttoM time sesolved analysis (TRA) software package. The software was used to identify background and active signals, as well as to calculate first-order statistics, including count rate averages, standard deviations, and statistical outliers (e.g., outside 3× the interquartile range). Subsequently, abundances were quantitated manually by correcting for instrumental drift (assuming a linear function) and converting count rates to concentrations, assuming 178 Hf as the internal standard.

Results

Low- Versus Medium-Resolution

Fractionation plots for each geological sample analyzed in low- (m/Δm = 300, 5% peak height) and medium-resolution (m/Δm = 2500, 5% peak height) are shown in Figure 2. In this type of diagram, discrepancies between published values of REE abundances in the suite of geological materials investigated here (Jochum et al. 2005) and those derived from this study are shown as deviations from unity (y = 1). Data points that plot above unity in any single sample material indicate a

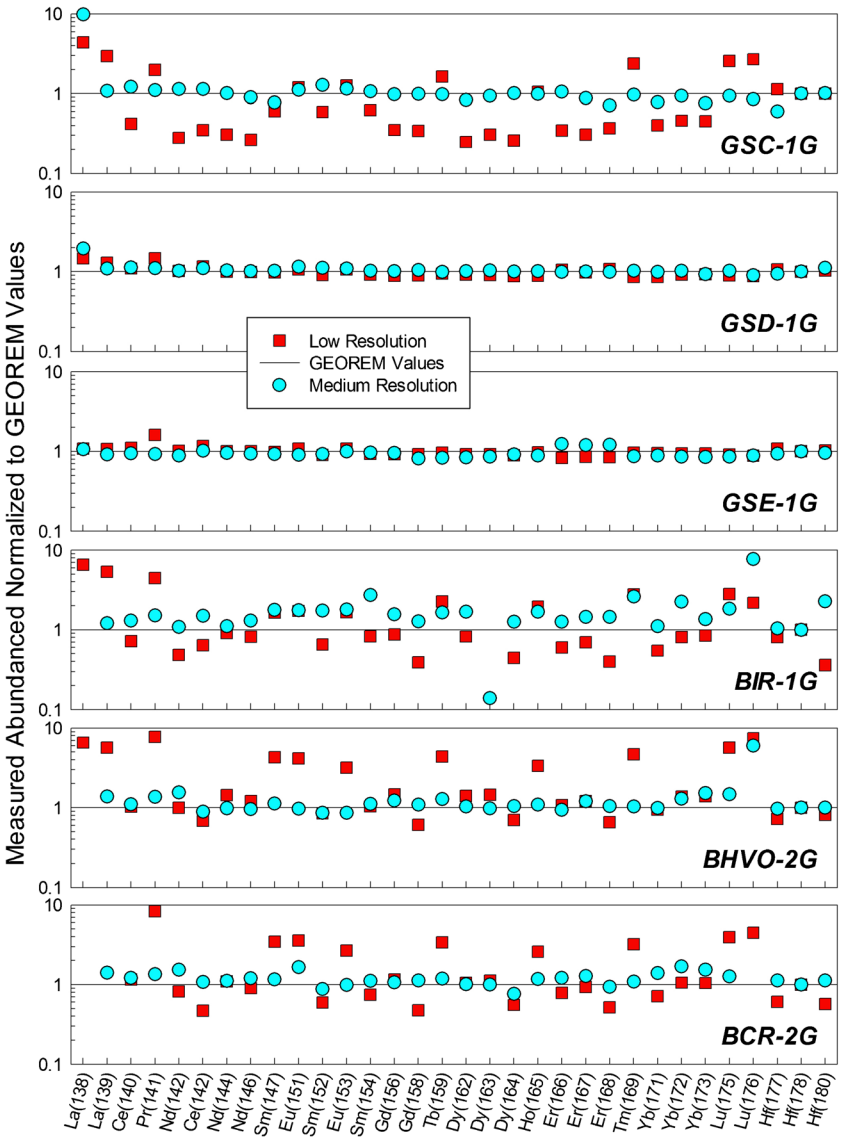

Figure 2. Comparison of quantitated REE abundances in the USGS reference glasses measured via low-resolution (m/Δm = 300 at 5% peak height) and medium-resolution (m/Δm = 2500 at 5% peak height) mass discrimination and compared with published values (Jochum et al. 2005). Significantly more scatter and larger absolute deviations in the data collected in low-resolution indicate isobaric interferences on the monitored mass stations (some of which is also observed in medium-resolution)

problematic isobar at that particular mass station in the analyte under those analytical conditions (i.e., mass discrimination). Conversely, data points that plot below unity suggest an isobar on that particular mass station in the bracketing reference material. See Appendix IV for complete results.

As shown in Figure 2, deviations between the quantitated values derived here and those found in the literature can vary by up to an order of magnitude in both low- and medium-resolution measurements at specific mass stations. These mass stations are plagued by isobaric interferences that require even greater mass resolving powers than those evaluated in this study, such as those outlined in Table 2. In nearly all cases, however, low-resolution measurements of the monitored mass stations deviate more intensely than those collected in medium-resolution. In particular, quantitated values of REE abundances collected in medium-resolution for GSC-1 g, BHVO-2 g, and BCR-2 g are significantly better aligned with the accepted published values for these elements. Some mass stations, such as 138 La, deviate significantly from the published values due to low relative abundances. However, for the majority of the mass stations, the low-resolution data set for these reference materials show variations between 0.3 and 3× published values, whereas the medium-resolution data generally fall within a few tens of percent.

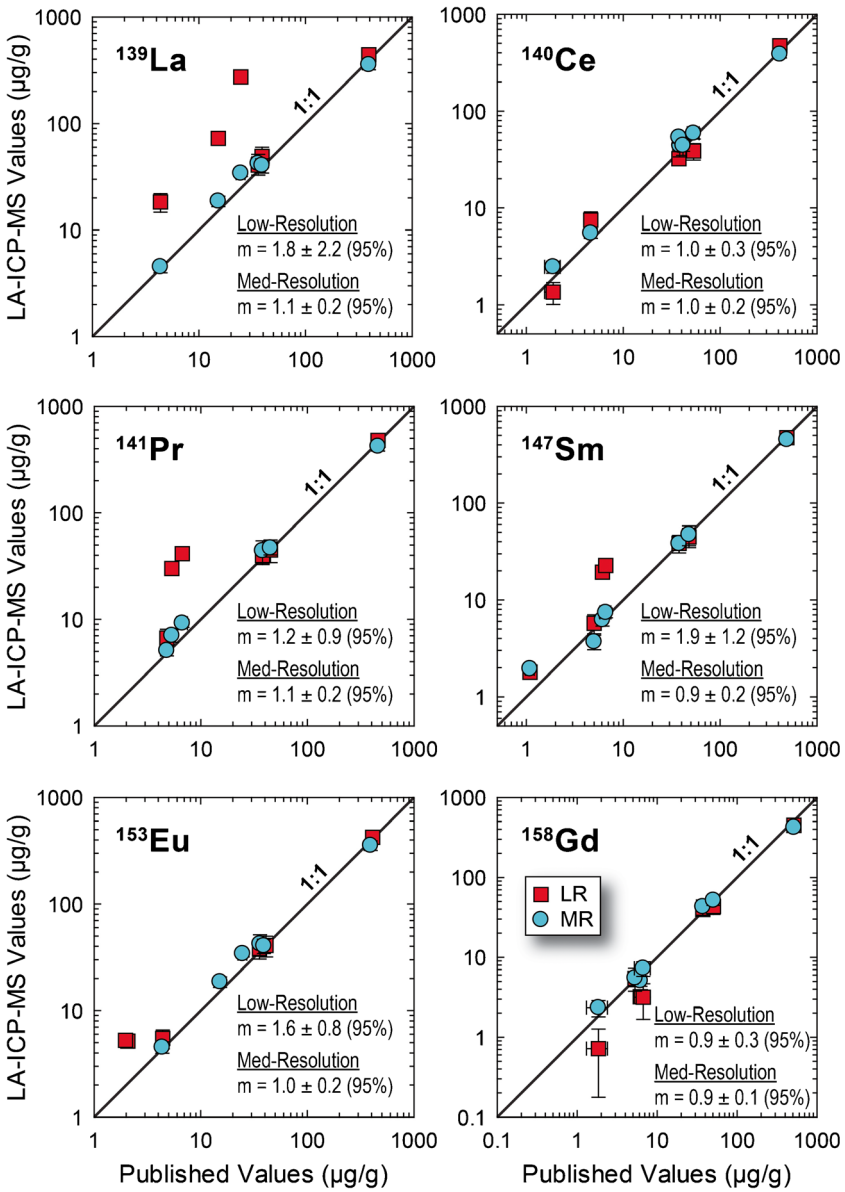

Figure 3. Accuracy of abundances measured here in low and medium-resolution. Error bars in the y-axis represent 2 sigma uncertainties on the external precision of four replicate measurements; error bars on the x-axis represent 95% confidence levels in the published values (Jochum et al. 2005). Statistics reported in each panel represent bivariate linear regression analyses, which incorporate analytical uncertainties in both x- and y-axis variables (unlike conventional univariate regressions). In this graphical representation, accuracy is manifest as a slope of unity (m = 1.0). Table I. LA-ICP-MS operational parameters employed during this study

Both low- and medium-resolution mass discrimination generate highly corroborative data in accord with published values for GSD-1 g and GSE-1 g. Because these samples are of the same lithology as GSC-1 g, the determined REE abundances of which are shown to be more sensitive to mass resolution, the uniform behavior of GSD-1g and GSE-1 g is likely due to their compositions enriched in incompatible trace elements, including the REE; elevated abundances of REE equate to higher counting rates, and by extension, reduced vulnerability to isobaric interferences. In contrast, significant scatter is seen with both resolving powers for BIR-1 g, the sample with the lowest concentrations of REE. In the case of BIR-1 g and other similarly depleted samples, counting statistics due to low REE abundances and limited count rates may ultimately limit the precision/accuracy of these measurements.

Ultimate Accuracy and Preferred Mass Stations

Medium-resolution mass discrimination is shown in Figure 2 to generate data that substantiate published values with equal or higher frequency compared with data collected via low-resolution techniques. In order to establish a more quantitative comparison, however, the absolute accuracies of both methods implemented here are evaluated in Figure 3. Best-fit bivariate linear regression statistics, which account for the uncertainties in both x- and y-coordinates (as opposed to conventional univariate least-squares methods), are provided for both the low- and medium-resolution data. In these types of graphical comparisons, a linear regression with a slope equal to unity (i.e., m = 1.0, within analytical uncertainty) indicates statistical uniformity between the data derived here and previously published data. As seen qualitatively (data point proximity to 1:1 line) and quantitatively (regression statistics) in these plots, data derived from medium-resolution mass discrimination correlate more closely with the REE abundances established in the literature compared with low-resolution data. More specifically, within analytical uncertainty (95% confidence envelope), the medium-resolution data acquired here are statistically indistinguishable from those determined by Jochum et al. (2005), which include measurements of multiple splits of both glass and powder of each material analyzed by LA-ICP-MS, isotope dilution ICP-MS, and isotope dilution thermal ionization mass spectrometry (TIMS). Although many of the linear regression analyses for the low-resolution data also coincide with a slope of m = 1 within uncertainty, the probability of these trend lines coinciding with a slope of unity is statistically less likely than the medium-resolution trend lines.

Based primarily on the fractionation plots discussed above (Figure 2) and bivariate linear regression statistics (Figure 3), in Table 2 we have derived a list of preferred mass stations to quantitate the abundance of each REE via LA-ICP-MS. Preference was given to mass stations with the highest isotopic abundance in order to emphasize higher counting rates and by extension achievable internal precision (Poisson statistics). Table 2 also provides representative compositions of an array of geological materials commonly analyzed for REE abundances, including chondritic materials, oceanic basalts, continental crust, and zircons of different genetic origins, in order to enable risk assessment for potential isobaric interferences.

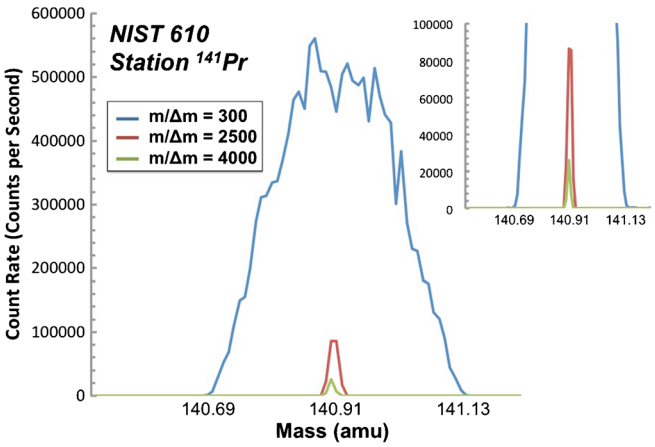

Figure 4. A representative spectra for ^{141}Pr is shown. The low-resolution (m/Δm = 300) collects the highest signal, but contains many unresolved isobaric interferences. Analyses at m/Δm = 2500 resolve many of these isobaric interferences without sacrificing as much signal as analyses at m/Δm = 4000

Conclusions

In situ LA-ICP-MS offers spatially resolved measurements of μm-size targets, such as individual minerals grains, while supporting minimal analytical blanks and low limits of detection. Moreover, such techniques avoid contamination risks associated with sample processing (e.g., high-temperature acid digestion, column chemistry, etc.) and consume orders-of-magnitude smaller quantities of sample (i.e., μg) compared with traditional solution techniques (i.e., mg). However, LA-ICP-MS methods are often complicated by isobaric interferences introduced during the ablation of the sample matrix, such as diatomic argides and oxides, particularly during the measurement of trace elements (i.e., μg/g level concentrations).

Here, we analyzed multiple isotopes of each REE with low- (m/Δm = 300, 5% peak intensity) and medium-resolution (m/Δm = 2500) mass discrimination in a suite of geological reference materials (i.e., BCR-2G, BHVO-2G, BIR-1G, and GSC/GSD/GSE-1G) in order to assess if higher mass resolving powers than those offered by quadrupole ICP-MS instruments are required for the highest precision/accuracy data. In summary, REE abundances quantitated from medium-resolution mass spectra are shown to be statistically equal (with 95% statistical confidence) to values established in the literature [18]; in contrast, data collected in low-resolution show significant deviations from published values, indicating spectral susceptibility to isobaric interferences (Figure 4).

Acknowledgements

Funding for this study was provided through the NASA Science Innovation Fund and Center for Research and Exploration

in Space Science and Technology (CRESST). R.F. acknowledges financial support from the Universities Space Research Association. R.F. also thanks Megan Elwood Madden for serving as a faculty sponsor, which enabled earning academic credit. R.A. Jr. acknowledges support from the NASA Astrobiology Institute (NAI) Cooperative Agreement Notice Cycle 7 (CAN7)

References

1. Hofmann, A.W.: Sampling mantle heterogeneity through oceanic basalts: isotopes and trace elements. Treatise Geochem. **2**, 568 (2003)
2. Workman, R.K., Hart, S.R.: Major and trace element composition of the depleted MORB mantle (DMM). Earth Planet. Sci. Lett. **231**, 53–72 (2005)
3. Arevalo Jr., R., McDonough, W.F.: Chemical Variations and regional diversity observed in MORB. Chem Geol. **271**, 70-85 (2010)
4. White, W.M.: Geochemistry. Wiley-Blackwell, Chichester (2013)
5. Hofmann, A.W.: Chemical differentiation of the Earth: the relationship between mantle, continental crust, and oceanic crust. Earth Planet. Sci. Lett. **90**, 297–314 (1988)
6. Sun, S., McDonough, W.F.: Chemical and isotopic systematics of oceanic basalts: implications for mantle composition and processes. Geol. Soc. Lond. Spec. Publ. **42**, 313–345 (1989)
7. McDonough, W.F.: Constraints on the composition of the continental lithospheric mantle. Earth Planet. Sci. Lett. **101**, 1–18 (1990)
8. McKenzie, D.: Some remarks on the movement of small melt fractions in the mantle. Earth Planet. Sci. Lett. **95**, 53–72 (1989)
9. MacPherson, G.J., Wark, D.A., Armstrong, A.: In: Kerridge, J.F., Matthews, M.S. (eds.) Meteorites and the early solar system, vol. 746. University Arizona Press, Tucson (1988)
10. Dauphas, N., Poitrasson, F., Burkhardt, C., Kobayashi, H., Kurosawa, K.: Planetary and meteoritic Mg/Si and variations inherited from solar nebula chemistry. Earth Planet. Sci. Lett. **427**, 236-248 (2015)
11. Trail, D., Watson, E.B., Tailby, N.D.: Ce and Eu anomalies in zircon as proxies for the oxidation state of magmas. Geochim. Cosmochim. Acta **97**, 70–87 (2012)
12. Goonan, T.: Geological Survey. Rare earth elements end use and recyclability. Scientific investigations report; 2011–5094. U.S. Dept. of the Interior, U.S. Geological Survey, Reston, Va (2011)
13. Palme, H., Jones, A.: Solar system abundances of the elements. In: Davis, A.M. (ed.) Meteorites, Comets and Planets, vol. 1, pp. 41-62. Elsevier-Pergamon, Oxford (2003)
14. Sun, S.S., McDonough, W.F.: Chemical and isotopic systematics of oceanic basalts; implications for mantle composition and processes. In: Saunders, A.D., Norry, M.J. (eds.) Magmatism in the ocean basins, vol. 42, pp. 313-345. Geological Society of London, London (1989)
15. Rudnick, R.L., Gao, S.: Composition of the Continental Crust. In: Rudnick, R.L. (ed.) The Crust, pp. 1-64. Elsevier-Pergamon, Oxford (2003)
16. Belousova, E., Griffin, W., O'Reilly, S.Y., Fisher, N.: Igneous zircon: trace element composition as an indicator of source rock type. Contrib. Mineral. Petrol. **143**(5), 602-622 (2002)
17. Russo, R.E.: Laser ablation. Appl. Spectrosc. Appl. Spectrosc. **49**, 14A–28A (1995)
18. Jochum, K.P., Nohl, U., Herwig, K., Lammel, E., Stoll, B., Hofmann, A.W.: GeoReM: a new geochemical database for reference materials and isotopic standards. Geostand. Geoanal. Res. **29**(3), 333–338 (2005)